RSC Advances

ROYAL SOCIETY OF CHEMISTRY

www.rsc.org/advances

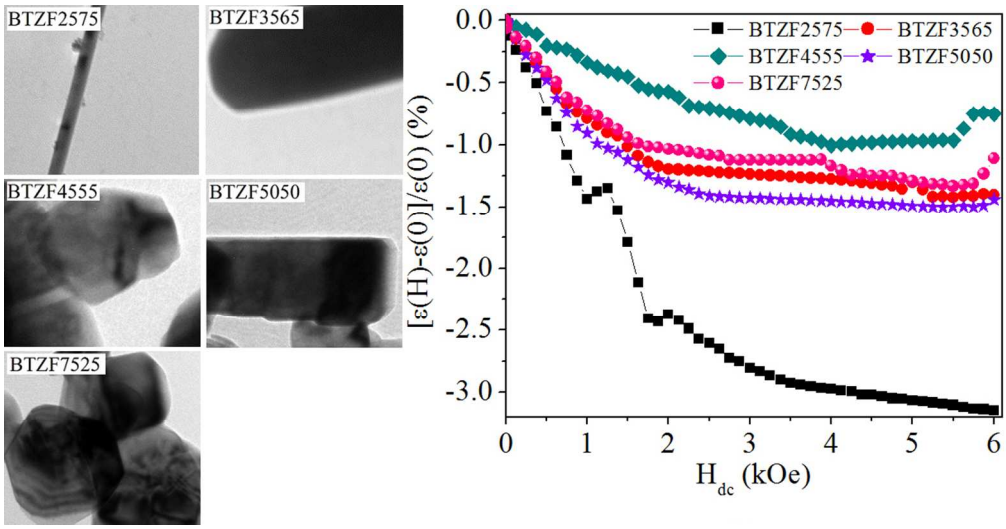

Magneto-electric/dielectric and photoemission of BTZF composites depends upon shape, size, surface spin, distortion, epitaxial strain etc. of nanostructure
320x166mm (96 x 96 DPI)

Magneto-electric/dielectric and Fluorescence effects in Multiferroic xBaTiO$_3$ - (1-x)ZnFe$_2$O$_4$ Nanostructures

[*]Kuldeep Chand Verma[1], S.K. Tripathi[1], R.K. Kotnala[2]

[1]*Centre of Advanced Study in Physics, Department of Physics, Panjab University, Chandigarh 160 014, India*
[2]*National Physical Laboratory, New Delhi 110012, India*

Abstract

Multiferroic composites of xBaTiO$_3$ - (1-x)ZnFe$_2$O$_4$ (BTZF) [x = 0.25 (BTZF2575), 0.35(BTZF3565), 0.45(BTZF4555), 0.50(BTZF5050) and 0.75(BTZF7525)] nanostructure have been synthesized by Sol-Gel method. Different types of nanostructural shape and size have been obtained by the effect of ionic radii, surface energy and PVA which enhances the magneto-electric/dielectric interaction between BT/ZF phases. The crystalline phases of BTZF composite are confirmed by X-ray diffraction, and nanostructural dimensions and shape by transmission electron microscopy. The improvement in magnetization of BTZF is depends upon size and shape of nanostructure, stoichiometric ratio and strength of occupation of cations at octahedral and tetrahedral sites. The chemical states of Fe in BTZF are analyzed by X-ray photoelectron spectroscopy. The ferroelectricity is explained by nano size effect, 1D nanostructure shape, lattice distortion and epitaxial strain between two phases. The magnetoelectric coefficient is measured at room temperature under an applied *dc* magnetizing field and show different types of behavior in each sample. The Magnetocapacitance is measured and explained on the basis of Maxwell-Wagner space charge and magnetoresistance, and relate with theoretical investigation which proves that the enhancement is not only depends on the size/shape of nanostructure but the strain-induced phase transition where out-of-plane polarization appears in the composite. The photoemission of BTZF is observed by Fluorescence spectra.

Keywords: A. Nanostructures; B. Magneto-voltage/capacitance; C. TEM; D. Photoemission

* Corresponding author. Tel.: +91 9418941286
E-mail: kuldeep0309@yahoo.co.in ; dkuldep.physics@gmail.com

1. Introduction

Multiferroic (MF) magnetoelectric (ME) nanostructural composites aimed at understanding new physics, such as product properties and dynamic coupling between electric and magnetic dipole moments [1], and microwave damping [2] – have attracted significance for magnetoelectronic and spintronic devices [3-5]. The ME coupling in MF composites is a strain mediated from electrical order in one phase to magnetic order in the other creates the desired ME phenomena [6]. The spin-current-based multiferroicity of MF composite is a interfacing ME coupling: Interfacing ferromagnetic (FM) with ferroelectric (FE) triggers in the FM low-energy (coherent magnonic) excitations near the interface, which builds up a spatially inhomogeneous, spin-current-carrying surface magnetic order within the spin-diffusion length (on the order of nm) [7]. These ME coupling contributes as: (ii) Quasistatic screening spins, which follow adiabatically the direction of local magnetic moments, yield a linear ME effect. (ii) Deviations from adiabaticity give rise to an exponential spiral spin density which goes along with an emergent electric response associated with the intrinsic spin current of the spiral [8]. In comparison of ME nanostructural composite to its bulk form, the FE and FM phases could be tuned and controlled at room temperature [9], whereas, the different phases can be combined at the atomic level, and thus interface losses could be reduced significantly results in an epitaxial or superlattice structure resides stress/strain [10].

The ME coupling manifests itself by electric properties on an applied magnetic field called direct ME effect is usually quantified in terms of the polarization and voltage coefficients. This polarization define the change δP by an applied magnetic field δH, as the magnetic-field control of electric polarization which terms as dynamic ME coefficient: $\alpha_E = \partial P/\partial H$ [11]. The associated output voltage δV induced by δH affects the dielectric properties of ME as well, additional important information on the degree of ME coupling is provided by

the Magnetodielectric coefficients. This can be easily evaluated by measuring the dependence of capacitance C on magnetic-field intensity is so called magnetocapacitance (MC) [11, 12]. The MC effect can be understood on the basis of Maxwell-Wagner space charge effect at the interface of composite and electrode or grain boundaries [13], and magnetoresistance.

Recently, perovskite based MFs composite such as $BaTiO_3$-$CoFe_2O_4$ [3,13], $BaTiO_3$/Fe [6], $ZnFe_2O_4$–$BaTiO_3$ [12], $BiFeO_3$–$CoFe_2O_4$ [14], $CoFe_2O_4$-$PbTiO_3$ [15], $LaCaMnO_3$/$BiFeO_3$ [16], $Pb(Zr_{0.52}Ti_{0.48})O_3$–$La_{0.65}Sr_{0.35}MnO_3$ [17], FeGaB/$Pb(La,Sn,Zr,Ti)O_3$ [18], $BaTiO_3$–$Ni_{0.7}Zn_{0.3}Fe_2O_4$ [19], $Ba_{0.8}Ca_{0.2}TiO_3$-$Ni_{0.2}Cu_{0.3}Zn_{0.5}Fe_2O_4$ [20] etc. have been widely investigated. Among them, the perovskite $BaTiO_3$ (BT) is a well-known [21] room-temperature ferroelectric that is tetragonal with $a = b = 3.99$ Å and $c = 4.03$ Å. At higher temperatures it is cubic and thus not ferroelectric, but on cooling it becomes tetragonal below the Curie temperature of 410 K [22], orthorhombic below 290 K and rhombohedral below 190 K. It is given in the recent report [23] that polycrystalline tetragonal BT nanostructure has enhanced polarization due to its twin structure in which stress resides near grain boundaries can easily controlled depolarization field and long range interactions. The nanostructural $ZnFe_2O_4$ (ZF) involves the redistribution of Fe^{3+} in to tetrahedral and Zn^{2+} in to octahedral interstices. This cationic rearrangement leads to the formation of two (A) and [B] magnetic sublattices, which are then responsible for the enhanced magnetization displayed when compared with bulk ZF [24, 25]. In order to obtain a high ME response in MF composites, the ferrite phase should be highly magnetostrictive possessing high resistivity which is possible in ZF nanostructure.

In comparison of nanoparticles and thin films, one dimensional (1D) nanostructures (nanorods, nanowires etc.) have special physical properties [26]. This is due to their anisotropic property and a unique size effect. Glinchuk *et al.* [27] pointed out that ferroic nanorods or nanowires will show giant ME effects as their radii decreases, and then induce an

abnormal increase in the dielectric tunability and dramatic phase transition. Moreover, M.Q. Cai *et al.* [28] were used first-principles calculation for the enhancement of spontaneous polarization as the polarization induce along length direction of wire by which the tension induced by nanowire surface curvature counteracts the near-surface depolarization effect.

In this paper we have synthesized MF composites of xBaTiO$_3$ - (1-x)ZnFe$_2$O$_4$ (BTZF) [x = 0.25 (BTZF2575), 0.35(BTZF3565), 0.45(BTZF4555), 0.50(BTZF5050) and 0.75(BTZF7525)] nanostructure by Sol-Gel method using poly vinyl alcohol (PVA) as surfactant. The structural, microstructural, ferroelectric, ferromagnetic, ME coefficient, magnetodielectric and fluorescence properties have been investigated.

2. Experimental detail

2.1. Preparation of BTZF nanostructures

For the synthesis of BTZF2575, BTZF3565, BTZF4555, BTZF5050 and BTZF7525 nanostructure, a typical simple chemical process, *i.e.*, Sol-Gel using PVA as surfactant was used. The precursor solution was prepared from barium acetate, tetra-n-butyl orthotitanate, zinc acetate and ferric chloride with desired molar concentration. In this method, ethanol and acetic acid were mixed in the ratio of 3:1. The tetra-n-butyl orthotitanate was added to it and stirred for 2h on magnetic stirrer marked as solution A. Barium acetate, zinc acetate and ferric chloride were dissolved in distilled water separately as a clear solution marked as solution B. The final solution M was prepared by mixing A and B drop wise and stirred for another 3h. This precursor solution, M was added in PVA solution in the molar ratio of M:PVA::5:2. The solution was dried at 250^{o}C and annealed at 700^{o}C for 2h to crystallize.

2.2. Characterization

Atomic absorption spectroscopy analysis was taken to check the composition of Ba, Ti, Zn and Fe content in BTZF using PerkinElmer system and both experimental and theoretical value of composition are well matched in each FE BT and FM ZF composite. The

crystalline structure was analyzed by X-ray diffraction (XRD) by using X'Pert PRO PANalytical system and microstructure by transmission electron microscopy (TEM) by using HITACHI H-7500. For electrical measurements, the BTZF crystalline powder was pressed into pellets of thickness ~0.5mm by the cold isostatic pressing method with a pressure of 5 bar for 10 min and then sintered at 1000 ^{o}C for 5 h. Polarization under the influence of applied electric field was measured using a Radiant Technologies FE test system. Magnetization of BTZF was measured at room temperature using Lakeshore 7304 vibrating sample magnetometer. The X-ray photoelectron spectroscopy (XPS) was performed using a Perkin Elmer model 1257 equipped with a nonmonochromatized Al Ka X-ray sources. The ME coupling coefficient was measured by the dynamic field method by a system built in-house. A buffer and high-pass filter circuit to reduce the background voltage noise are employed in the measurement set-up to detect the induced ME voltage across the sample thickness. The room temperature magnetodielectric performed on BTZF samples at frequency of 1 kHz by change in relative dielectric permittivity as a function of an applied magnetic field strength, was measured by combining a Wayne Kerr 6500B Precision Impedance analyzer with the Lakeshore 7304. The photoemission is shown by fluorescence spectrum of BTZF was recorded using Edinburgh FLSP920 spectrofluorophotometer at room temperature.

3. Result and discussion

Figure 1 show the XRD patterns of all samples of BTZF composites measured at room temperature. The pattern confirms the existence of two phases namely perovskite and spinel together corresponding to BT and ZF, respectively. The polycrystalline BT of tetragonal phase at diffraction angle 2θ = 21.74, 22.66, 31.71, 39.27, 44.73, 51.75 and 56.01 are corresponds to (001), (100), (101), (111), (200), (102/201) and (112/211) respectively, observed. The reflections 001/100 and 102/201 are the splitting of cubic into tetragonal

phase. While for 2θ = 29.69, 35.27, 36.84, 42.78, 48.73, 53.45 and 58.67^o are corresponds to (220), (311), (222), (400), (331), (422) and (511), respectively, indicates cubic spinel phase of ZF. Using the CHEKCELL lattice constant refinement program, the lattice parameters of both phases are summarized in Table 1. The distortion ratio *c*/*a* of tetragonal BT is 1.0494, 1.0087, 1.0076, 1.0089 and 1.0097, respectively, calculated for BTZF2575, BTZF3565, BTZF4555, BTZF5050 and BTZF7525 composite. The distortion, *c*/*a* when compared with pure BT (*c*/*a*~1.01) [21], 75%BT in BTZF has slightly smaller value of *c*/*a* and decreases with decreasing BT to 45%BT. The smaller *c*/*a* value of BT phase in the composite than pure BT ceramic suggests the diffusion of Fe^{3+} or Zn^{2+} into the BT lattice from the ZF phase. $BaTiO_3$ is known to enable substitution of different sizes of ions including Fe^{3+} and Zn^{2+} and the doping/substitution site depends on the size of the ions [29]. The ionic radii of Fe^{3+} (0.69 Å) and Zn^{2+} (0.88 Å) are comparable to the ionic radius of Ti^{4+} (0.745 Å) than Ba^{2+} (1.49 Å) and therefore, Fe^{3+} and Zn^{2+} substitution will occur at the Ti-site [30]. While substitution of Fe^{3+} can result in a decrease of BT lattice parameters because of its smaller radius than Ti^{4+} [18]. Zn^{2+} substitution, on the other hand, can increase the BT lattice parameters due to its larger ionic radius than Ti^{4+}. Therefore, with 25%BT in BTZF has large value of lattice distortion because Zn^{2+} is reach and larger ionic radius than both Fe^{3+} and Ti^{4+}. Moreover, substitution of Zn^{2+} and Fe^{3+} at Ti^{4+} sites will cause in the formation of oxygen vacancies to maintain the electroneutrality [30] and this oxygen vacancies contribute to the increase of the lattice parameters.

Figures 2 (a & b) shows the TEM images (left) and HRTEM images (right) of BTZF nanostructural composites measured at different magnification because the shape and size of nanostructure (nanoparticles, nanowires and nanorods) in each sample is quite different and create difficulty to visualize the clear picture of shape and size at same magnification apply in each samples. The BTZF2575 composite form nanowire like structure of average diameter

(*d*) is 6 nm and length is greater than 100 nm. But with increasing BT concentration the dimensions along length side decreases and the diameter show an increment, *i.e.*, the formation of nanorods like structure. The average value of *d* is 33, 54 and 59, and *l* is 103, 120 and 141 nm, respectively, measured for BTZF3565, BTZF4555 and BTZF5050 nanorods. However, the BTZF7525 composite form nanoparticles of cubic type shape and the average value of *d* is 84 nm. The mechanism in the formation of nanoparticles, nanorods and nanowire is explained in the next paragraph. It has been also observed in the TEM images that there are random distribution of dark and bright border which are may be the formation of FE BT and FM ZF phases alternatively into a single nanocrystal is clearly shown by HRTEM image on right portion of Figs. 2(a & b). Large regions of periodically ordered material are no longer observed, indicating randomly filling of phases. This type of the behavior to imagine the two phase in a single crystal is described recently by Sreenivasulu *et al.* [31]. The planes with interplanar spacing, $d \sim 0.28$ nm of most intense peak (101) of BT in the XRD pattern is observed in all HRTEM images and $d\sim 0.25$ of most intense peak (311) of ZF is also seen. In BTZF2575, the most frequently lattice fringes are oriented parallel to the major axis of the nanowires. The high crystallinity of the particles is evident from the selected area electron diffraction SAED pattern shown in the insets of HRTEM images and shows that all the composites are of polycrystalline phase.

The formation of different types of nanostructural (nanoparticles, nanorods and nanowires) formation is explained on the basis of ionic radii, surface energy and PVA acts as surfactant as well as orientation during growth process of large aggregates of metal ions. The variation in the size of grains is due to different ionic radii of metal ions and their stoichiometric ratio is different in each BTZF composite. The variation in the shape of BTZF nanostructure is explained on the basis of surface energy of Zn^{2+} ion which is higher and form agglomeration process during chemical reaction with OH^- ion [32]. The Zn^{2+} ion in OH^-

medium form normally divalent metal ions and their solubility increases with appropriate concentration and temperature. During heating, the surfactant PVA helps in synthesizing nanostructure. Under heat treatment of PVA, there exist two sites namely hydrophobic (Hb) and hydrophilic (Hp) of PVA and form clusters. The Hb keeps the materials separate due to their repulsive forces which slowdown the rate of reaction. Where Hp keeps the metal intact and retards the growth process. Therefore, higher concentration of Zn^{2+} ions form large agglomeration with OH^- and when this product react with PVA, the Hp site gives the orientation to grow continuously in the confined reverse micelles process causing formation of nanorods and nanowires. Moreover, the Ostwald ripening theory [32] is also responsible for this type of crystal growth process.

Figure 3 (a-e) shows the FM behavior of BTZF composites by measuring magnetization versus applied magnetizing field (M-H_{dc}) hysteresis at room temperature. The values of saturation magnetization (M_s) are 0.19, 15.41, 8.71, 0.15 and 0.25 emu/g, and remanent magnetization (M_r) are 0.056, 3.19, 1.38, 0.038 and 0.047 emu/g, and coercive field (H_c) are 1068, 319, 255, 249 and 116 Oe respectively, measured for BTZF2575, BTZF3565, BTZF4555, BTZF5050 and BTZF7525 composite and are also given in Table 1. These values of ferromagnetism observed improvement than reported work on BT based MF composites [12, 19, 20, 33-35]. The variation of observed ferromagnetism with BT concentration in BTZF is shown in Fig.3 (f). The value of magnetization is slightly varied with 25, 50 and 75% of ZF concentration in BTZF but increase abruptly with 55 and 65% of ZF. This type of the behavior is explained on the basis of size and shape of nanostructure, and stoichiometric ratio of MF BTZF composite. The slight variation in ferromagnetism is the general behavior which depends upon the size of nanograins [32]. The shape of nanostructure is also responsible for improvement in M_s. Since the nanostructure is increase the strength of magnetic exchange interaction by surface spins contributed by their large surface to volume

ratio and involves a similar behavior given by Callsen *et al.* [36] for nonmagnetic organic molecules on the FM surface using theoretical first principle calculations. In BTZF nanostructure, the nonmagnetic nano boundaries between nanograins are present instead of organic molecules. It is demonstrated that the possibility of a hybrid nano boundaries - FM interface acts as a local embedded surface spin based magnetic unit due to a magnetic hardening of BT in the composite and exhibit spin-filter functionality with sharp spin split molecular like electronic features at nano boundaries site. This surface spin induced local magnetic hardening leads to exchange interactions and therefore, a larger magnetic anisotropic energy results in a stable magnetization axis. This type of magnetism by surfaces and interfaces of nonmagnetic nano boundaries is also described by Neeleshwar *et al.* [37] for Ge quantum dots. As discussed above, it is concluded that the orbital momentum induced at the surface conduction electrons is crucial to understand the observed giant anisotropy.

The abrupt increment of M_s in BTZF3565 and BTZF4555 [Fig.3 (f)] composite is also seen in various ferrites and MFs system based on ZF [25, 38]. Generally in ZF, the magnetic properties are strongly dependent on the strength of occupation of various cations at octahedral and tetrahedral sites. It is well known that in nanostructural ZF, the antiferromagnetic ordering temperature is much higher (T_N = 450 K) [25] can be raised by increasing the Fe^{3+} occupation at the tetrahedral sites through mechanical activation. This increase of magnetization originates in the stronger inter sub-lattice (A-B) superexchange interaction as compared to intra sub-lattice (A-A and B-B) interactions. At lower ZF concentration, A-A and B-B interactions are dominant. But with higher concentrations, *i.e.*, 50 - 60% ZF in BTZF, Fe^{3+} occupy Ti^{4+} along B site of perovskite via oxygen vacancy and hence stronger the superexchange A-B interactions which results in an abrupt increment in magnetization. With sufficient higher concentration, 75% of ZF, weakening of the A-B exchange interaction and the parallel orientation of the magnetic moments in B-site is altered

that compensate each other only partially which leads to a progressive decrease of saturation magnetization.

In order to find the contribution of Fe on ferromagnetism of BTZF composites, the XPS spectra has been given in Fig.4 measured at room temperature for Fe 2p states in the binding energy region 700 – 727 eV. It was reported [39] that Fe 2p photoelectron peaks from oxidized iron are associated with satellite peaks, which is important for identifying the chemical states. The Fe^{2+} and Fe^{3+} $2p_{3/2}$ peaks always show the satellite peaks at 6 eV and 8 eV above the principal peaks at 709.5 eV and 711.2 eV, respectively [39]. In Fig. 4, the satellite peaks were found in the energy region of 6-8 eV above $2p_{3/2}$ principal peak. It indicates that in this BTZF MF system Fe is coexists into both Fe^{2+} and Fe^{3+} states. When Fe^{3+} ion coexist with Fe^{2+} in ZF, the Fe^{3+} distort the lattice structure more than Fe^{2+} ion due to the effects of charge and ionic size [40]. The difference in energy between the Fe $2p_{3/2}$ and $2p_{1/2}$ peaks resulting from spin-orbit coupling is ~ 13.5 eV which is very close to the reported value of Fe 2p [39]. The peaks related to $2p_{3/2}$ are 710.16, 709.83, 710.07, 710.05 and 710.16 eV, and $2p_{1/2}$ are 723.67, 723.34, 723.59, 723.37 and 723.92 eV, respectively, observed for BTZF2575, BTZF3565, BTZF4555, BTZF5050 and BTZF7525 composite. These results suggest that the Fe ions have mixed valence state of 2+ and 3+ and must be contributes ferromagnetism via oxygen vacancy.

The insets of Fig. 3 (a-e) show the polarization versus electric field (*P*-*E*) hysteresis curves at room temperature on poled sample of BTZF composites with 50 Hz the frequency of polarization. The values of spontaneous polarization, P_s = 69.61, 41.95, 26.31, 31.66 and 26.18 μC/cm^2, and remanent polarization, P_r = 18.44, 5.47, 5.36, 6.41 and 12.51 μC/cm^2, and coercive field, E_c = 13.79, 1.78, 3.61, 12.81 and 13.93 kV/cm, respectively, measured for BTZF2575, BTZF3565, BTZF4555, BTZF5050 and BTZF7525 composite and are also given in Table 1. These values of polarization show improvement than reported work of BT based

MF composites [12, 13 17, 20, 33, 41]. The values of P_r are plotted in Fig. 3(f) with varying BT concentration and shows abrupt decrement for BT>0.25 and again enhanced for BT ≥0.5. This improvement and increment in the value of P_r is depends upon different factors, *i.e.*, nanosize, 1D nanostructural formation, lattice distortion and epitaxial strain [23, 28] and the resulting mechanism is described by arguments: the suggestion by Lu *et al.* [42] is also apply on BTZF nanostructural composite which is associated with multidomains, the ZF certainly induced modifications onto the FE properties of BT, which might be change the depolarization field including change in interfacial strain via magnetostriction effect. However, the stability of ferroelectricity in nanoscale BT is proposed by Spanier *et al.* [43] on the basis of polarization-induced surface charges. Incomplete screening of surface charges by nanostructure results in a depolarization field that opposes the bulk polarization, thereby suppressing ferroelectricity. When the nanostructural formation in the forms of rods and wire, the capacitive contribution eliminates between the tip and the length so that the resulting map exhibits only the contribution from the surface charges associated with a local electric polarization. Moreover, the BTZF nanostructure is synthesized by Sol-Gel based chemical process where may be the possibility of the presence of OH ions on the surfaces. These molecular adsorbates OH ions can compensate the surface polarization charges, providing a mechanism for reducing the depolarizing fields [43]. The BTZF nanostructure exist both Fe^{2+}/Fe^{3+} ions [Fig.4] which makes the possibility that each Fe^{2+} with its surrounding Fe^{3+} will form a dipole with strong local polarization. Under an external electric field, the hopping of electrons between Fe^{2+} and Fe^{3+}, which is equivalent to the reversal of the dipole, contributes to the large polarization and involves a similar behavior observed in nano MF $YFeO_3$ [44]. Furthermore, the jumping of electrons in Fe^{2+}/Fe^{3+} dipoles is also a switching process of the dipole, which contributes to magnetocapacitance effect [Fig.6] due to the jumping getting easier in magnetic field [44].

The ME coupling coefficient was determined as a function of dc magnetic field using equation as [11]:

$$\alpha_E = \frac{\partial E}{\partial H} = \frac{1}{t}\frac{\partial V}{\partial H} = \frac{V_{out}}{t \times H_{ac}} \quad (1)$$

where t is the sample thickness and V_{out} is the induced ME voltage. The variations in α_E with H_{dc} at *ac* magnetic field frequency of 1093 Hz and *ac* magnetizing field of 5 Oe for BTZF nanostructure is shown in Fig. 5. In these cases, the ME effect results from the interaction between different orderings of the two phases in the composite. This is an interface coupled electrical and magnetic ordering via elastic interaction between the piezoelectric and piezomagnetic phases [45]. There is an elastic coupling at the interface (randomly distributed BT and ZF): an applied magnetic field produces an elastic strain in the magnetostrictive phase (ZF), which is stress coupled to that of the piezoelectric (BT), resulting in an induced voltage. Moreover, Bary'achtar *et al.* [46] reported that an electric polarization appears in the vicinity of the inhomogeneous magnetic media due to the lowering of the magnetic symmetry group of the crystal. In this context, the absence of a symmetry centre in the near-interface should lead to an extra ME effect at the interfaces in the composite. The value of α_E at H_{dc} = 3 kOe is 122.9, 30.5, 29.2, 51.7 and 43.9 mV/cmOe, respectively, measured for BTZF2575, BTZF3565, BTZF4555, BTZF5050 and BTZF7525 composite. These values of α_E show improvement than reported work on BT based MFs composite [3, 19, 20, 33, 34, 47, 48] which is depends upon: (i) the surface spins of nanostructure enhances magnetostriction constant (λ), $\lambda_{total} = \lambda_{bulk} + \lambda_{surf}/t$ [49] due to the reduced symmetry of atoms on the surface. The large surfaces of nanorods and nanowires results Giant electric field tuning of the magnetic anisotropy, FM resonance field, coercive field and anisotropic magnetoresistance were demonstrated. (ii) In 1D nanostructure, long range interaction is truncated due to the lack of periodicity and short range one is significantly modified near the surface boundary [50]. The compressive stress induced by surface curvature of nano rods/wire would produce

an effective tensile in the length direction leads to a big off-center displacement which enhance induced ME voltage. (iii) BTZF nanostructure of highly distorted BT polycrystalline phase contributes twin structure where the stress resides near grain boundaries lead to enhance ME polarization [10]. And, (iv) the epitaxial strain by lattice mismatch of FE and FM phases. The observed ME response is varying non-linearly and do not have abrupt decay of α_E by varying H_{dc} is explained by the mechanism given by A. Sukhov *et al.* [6] in BT composites of tetragonal phase. It is suggested that this MF contact consisting of a thin FM ZF layer and a thick FE BT. The thin FM layer responsible for spin waves as well as to avoid a decay of the ME coupling in long FMs, whereas the thick FE part stabilizes the FE polarization. Because the interfacial screening charges due to epitaxial growth with highly distorted BT tetragonal phase, the principal axis of ZF is rotated by 45^o [6].

The origin of ME coupling of BTZF composite is the coupling of FE and FM degrees of freedom due to the influence of FE matrix on the exchange coupling constant via screening of the intragrain and intergrain Coulomb interaction. Therefore, a possible mechanism for ME coupling of this FE/FM (BTZF) interface is based on screening effects [51]. The spin-polarized charge density formed in the FM in the vicinity of the FM/FE interface [52] acts with a torque on the magnetic moments in the FM, resulting in a noncollinear magnetic ordering [53]. Hence, electric polarization emerges that couples the FM to the FE part. Additionally, the FE polarization (and electric field) stems actually from the FE surface which triggers the spin spiral in a FM. The latter carries a spin current with an associated Aharonov-Casher effect and/or Dzyaloshinkii-Moriya (DM) interaction [54]. In this sense the ME coupling caused by an emergent inverse DM interaction at MF interfaces [7].

Recently, MF composite has MC or magnetodielectric (MD) effects [11,12], where composite with inhomogeneous structures in the interfacial layers for different resistivity and other electric structures, MR value could be calculated with a simple equivalent circuit of two

parallel RC elements in series. MR depends upon core-based and the interfacial (nanograins boundaries) of MF composite [12]. For MF composite under an external magnetic field, the magnetostriction in the magnetic phase produces stresses transferred in the FE phase, resulting in an electric polarization via the ME effect [12]. As a result, the dielectric behavior is modified. The MC/MD is the change in dielectric constant (ε), $[\varepsilon(H) - \varepsilon(0)]/\varepsilon(0)$, where $\varepsilon(H)$ and $\varepsilon(0)$ denotes the dielectric constants at applied magnetic field H and zero field. Figure 6 shows the change in the real part of the relative dielectric permittivity of the nanostructural BTZF composites at 1 kHz as a function of magnetic field H_{dc} and measured at room temperature. Clearly, the capacitance decreases with increasing applied magnetic field (negative value of MC) and a similar behavior is also observed by Anjum *et al.* [55] for their MF system. The value of MC at H_{dc} = 3 kOe is 2.84, 1.24, 0.78, 1.42 and 1.12%, respectively, calculated for BTZF2575, BTZF3565, BTZF4555, BTZF5050 and BTZF7525 composite.

Pertsev *et al.* [11] gives theoretical calculations of strain-mediated MC of $BaTiO_3$ film deposited on FM substrate show a similar behavior as observed in the present BTZF nanostructure where ME coupling is mediated via lattice strains. It has been observed for BT films that the lattice mismatch $S^{\varepsilon}_{\alpha\alpha}(u_m = -1\%) \cong 43$ and $S^{\varepsilon}_{\alpha\alpha} = (u_m = +1\%) \cong -58$, where $S^{\varepsilon}_{\alpha\beta}$=$S^{\varepsilon}_{\alpha\beta}(u_m)$ of the out-of-plane permittivity ε_{33} as a function of the initial biaxial strain u_m. In the present case, BT has tetragonal phase with higher tetragonal distortion and ZF of cubic. Therefore, these values of $S^{\varepsilon}_{\alpha\alpha}$ may be improved at different types of nanostructural formation of BTZF [56].

For these strain - mediated ME effect in a MF composite, the coefficient can be calculated as

$$\alpha^{\varepsilon}_{ijk} = \frac{\partial \varepsilon_{ij}}{\partial u_{11}} \frac{\partial u^{S}_{11}}{\partial H_k} + \frac{\partial \varepsilon_{ij}}{\partial u_{22}} \frac{\partial u^{S}_{22}}{\partial H_k} + \frac{\partial \varepsilon_{ij}}{\partial u_{12}} \frac{\partial u^{S}_{12}}{\partial H_k} \qquad (2)$$

where $u_{\alpha\beta}$ (α, β = 1,2) are the in-plane composite strains and deformation, respectively, and the perfect mechanical coupling at the FE/FM (BT/ZF) interface is assumed ($\delta^{u}_{\alpha\beta} = \delta^{S}_{\alpha\beta}$). Since the deformation response of a FM material to be weak measuring magnetic field δH becomes linear under sufficient bias field H, the second term in (2) can be replaced by the interface field-dependent piezomagnetic coefficients $d^{m}_{j\alpha\beta} = \partial u^{S}_{\alpha\beta}/\partial H_j$. It should be emphasized that the local deformation response of interface region beneath the BT nanostructure which generally depends upon the geometry of interface.

Indeed, when the magnetic field is not parallel to the composite interface, the demagnetising field evenly makes $d^{m}_{3\alpha\beta}$smaller than the piezomagnetic coupling where the internal magnetic field is equal to the applied one. Consider BTZF as parallel plate capacitor, where only the out-of plane composite permittivity ε_{33} is important. Introducing the strain sensitivities $S^{\varepsilon}_{\alpha\beta}$ of the permittivity ε_{33} via the relation $\delta^{\varepsilon}_{\alpha\beta} = \partial ln\varepsilon_{33}/\partial u_{\alpha\beta}$, the resulting product as obtained:

$$MC = \frac{\varepsilon_{33}(\delta H) - \varepsilon_{33}(0)}{\varepsilon_{33}(0)}$$

$$\cong \sum_{j=1}^{3} (S^{\varepsilon}_{11}\, d^{m}_{j11} + S^{\epsilon}_{12} d^{m}_{j12} + S^{\epsilon}_{22} d^{m}_{j22}) \delta H_i \qquad (3)$$

This equation (3) valid for weak fields $\delta H \ll H$ that do not change the initial piezomagnetic coefficients and strain sensitivity significantly. Therefore, sensitivities $S^{\epsilon}_{\alpha\beta}$ can be calculated using the non-linear thermodynamic theory [57, 58] by neglecting the in-plane lattice strain [11]. When the composite stabilizes in the tetragonal *c* phase ($P_1 = P_2 = 0$, $P_3 \neq 0$) the strain-mediated MC appears to be significant and there is no direct proportionality between the MC and the ME voltage coefficient. Therefore, it gives a contrast between the MC and ME voltage coefficient which may becomes negligible at $P_3 = 0$ in the conventional

parallel plate capacitor geometry of BTZF nanostructures where BT and ZF are distributed over randomly separated by a buffer layer of nano grain boundaries.

In the case of *aa* phase ($|P_1| = |P_2|, P_3 = 0$) formed an isotropic biaxial strain (u_{11} = u_{22} = u_m, u_{12} = 0), by measuring magnetic field δH does not induce shear strain u_{12} in the composite [9] is sufficient to calculate the strain mediated MC using (3).

Therefore, to evaluate MC of ME composite, we need to know only the longitudinal piezomagnetic coefficient characterizing the deformation u_{11}^S induced along the field direction and the transverse coefficient governing the deformation $u_{\perp}^S$ in the direction orthogonal to δH. Considering $d_{\parallel}^m$ and $d_{\perp}^m$, we obtain,

$$MC = \left[S_{\parallel}^{\varepsilon}\left(d_{\parallel}^m + d_{\perp}^m\right) - \frac{1}{2}S_{12}^{\varepsilon}\left(d_{\parallel}^m - d_{\perp}^m\right)sin2\varphi\right]\delta H \qquad (4)$$

where φ is the angle between the magnetic field δH and the [100] crystallographic axis of BT. The theoretical calculate MC/δH of BT interface is ~10^{-4} Oe^{-1}. The measured values of MC from Fig. 6 are given in table 1 are consistent with above theoretical observation. This is the giant MD effect has potential applications in advanced electronic devices.

Figure 7 shows fluorescence spectrum of BTZF nanostructures measured at room temperature. The absorption bands due to Green centred at 555.48 and 563.33 nm, and red at 646.42 and 674.84 nm are observed. The green luminescence is distinctly enhanced in BTZF 2575, 7525 and 5050 nanostructure. However, the emission intensity is enhanced for BTZF7525. The generation of oxygen vacancies in the lattice leaded to the shrink of the lattice [59, 60]. The distortion of the local asymmetry along B-site of BT increases, and the transition probabilities which govern various intra - shell transitions giving rise to both green and red emission are increases [59]. As a whole, the enhanced luminescence is conjectured to result from the distortion of the local asymmetry and oxygen vacancy generated by Fe^{3+} ion incorporation in the Ti^{4+} lattices [60]. The absorption bands, *i.e.*, 279.57, 340.78 and 352.58

nm are lying in the UV emission which is related to near band emission attributed to free-exciton recombination [61].

4. Conclusion

The MF BTZF composites were synthesized by Sol-Gel process at 700 ^{o}C/2h using PVA as surfactant result in nanorods, nanowires and nanoparticles type nanostructural formation which enhances the ME coefficient and MC response. The XRD results show coexistence of polycrystalline phases, *i.e.*, tetragonal and spinel, respectively, for BT and ZF. The tetragonal distortion of BT phase depends upon the size and concentration of composite ions, and oxygen vacancies. The nanostructures of BTZF2575 form nanowires while BTZF3565, BTZF4555 and BTZF5050 are nanorods and BTZF7525 form nanoparticles. The mechanism in the formation of nanoparticles, nanorods and nanowire is explained on the basis of ionic radii, surface energy, PVA and Ostwald ripening process. The XPS analysis results in mixed valence state of 2+ and 3+ of Fe in each BTZF sample. The values of M_s = 0.19, 15.41, 8.71, 0.15 and 0.25 emu/g, and P_s = 69.61, 41.95, 26.31, 31.66 and 26.18 μC/cm^2, and α_E (at H_{dc} = 3 kOe) = 122.9, 30.5, 29.2, 51.7 and 43.9 mV/cmOe, and MC (at 1 kHz frequency and H_{dc} = 3 kOe) = 2.84, 1.24, 0.78, 1.42 and 1.12%, respectively, measured for BTZF2575, BTZF3565, BTZF4555, BTZF5050 and BTZF7525 nanostructural composite. The enhancement in ME and MD is possible by strain-mediated magnetocapacitance exist on the basis of nonlinear thermodynamic theory can be exploited in magnetic-field-controlled ferroelectric capacitors namely magnetovaractors implemented in electronic oscillators, where the oscillation frequency is tuned by a *dc* magnetic field remotely (via the change of capacitance) in contrast to conventional voltage-controlled oscillators.

References

1. W. Eerenstein, M. Wiora, J.L. Prieto, J.J. Scott and N.D. Mathur, *Nature Mater.*, 2007, **6**, 348.

2. C. Brosseau, V. Castel and M. Potel, *J. Appl. Phys.*, 2010, **108**, 024306.

3. Y. Shen, J. Sun, L. Li, Y. Yao, C. Zhou, R. Su and Y. Yang, *J. Mater. Chem. C*, 2014, **2**, 2545

4. J. Wu and J. Wang, *J. Appl. Phys.*, 2009, **105**, 124107

5. J. Wu and J. Wang, *Electrochem. Solid-State Lett.*, 2009, **12(10)**, G61

6. A. Sukhov, P.P. Horley, C.L. Jia and J. Berakdar, *J. Appl. Phys.*, 2013, **113**, 013908.

7. C.L. Jia, T.L. Wei, C.J. Jiang, D.S. Xue, A. Sukhov and J. Berakdar, *Phys. Rev. B*, 2014, **90**, 054423

8. M. Mostovoy, *Phys. Rev. Lett.*, **2006**, 96, 067601

9. Y. Wang, J. Hu, Y. Lin and C.W. Nan, *NPG Asia Mater.*, 2010, **2(2)**, 61.

10. M.H. Frey and D.A. Payne, *Phys. Rev. B*, 1996, **54**, 3158

11. N.A. Pertsev, S. Prokhorenko and B. Dkhil, *Phys. Rev. B*, 2012, **85**, 134111.

12. M. Lorenz, M. Ziese, G. Wagner, J. Lenzner, C. Kranert, K. Brachwitz and M. Grundmann, *Cryst. Eng. Comn.*, 2012, **14**, 6477.

13. J.S. Andrew, J.D. Starr and M.A.K. Budi, *Scripta Materialia*, 2014, **74**, 38

14. F. Yan, G. Chen, L. Lu, P. Finkel and J.E. Spanier, *Appl. Phys. Lett.*, 2013, **103**, 024906.

15. C.Y. Tsai, H.R. Chen, F.C. Chang, H.H. Kuo, H.M. Cheng, W.C. Tsai, Y.H. Chu, C.H. Lai and W.F. Hsieh, *J. Appl. Phys.*, 2014, **115**, 134317.

16. D. Yi, J. Liu, S. Okamoto, S. Jagannatha, Y.C. Chen, P. Yu, Y.H. Chu, E. Arenholz and R. Ramesh, *Phys. Rev. Lett.*, 2013, **111**, 127601.

17. X. Lv, C. Cheng, Y. Yiao, M. Tang, Z. Tang, H. Cai, Y. Zhou and R. Li, *Mater. Lett.*, 2013, **100**, 7.

18. Z. Zhou, X.Y. Zhang, T.F. Xie, T.X. Nan, Y. Gao, X. Yang, X.J. Sun and D.Z. Sun, *Appl. Phys. Lett.*, 2014, **104**, 012905.

19. R.F. Zhang, C.Y. Deng, L. Ren, Z. Li and J.P. Zhou, *Mater. Res. Bull.*, 2013, **48**, 4100

20. K. Sadhana, S.R. Murthy, S. Jie, Y. Xie, Y. Liu, Q. Zhan and R.W. Li, *J. Appl. Phys.*, 2013, **113**, 17C731.

21. H.F. Kay and P. Vousden, *Phil. Mag.*, 1949, **40**, 1019.

22. A.M. Bratkovsky and A.P. Levanyuk, *Phys. Rev. Lett.*, 2005, **94**, 107601

23. K.C. Verma, J. Kaur, N.S. Negi and R.K. Kotnala, *Solid State Comn.*, 2014, **178**, 11.

24. K.C. Verma, V.P. Singh, M. Ram, J. Shah, R.K. Kotnala, *J. Magn. Magn. Mater.*, 2011, **323**, 3271.

25. M. Atif, S.K. Hasanain, and M. Nadeem, *Solid State Commun.*, 2006, **138**, 416.

26. B. Liu, B. Hu and Z. Du, *Chem. Comm.*, 2011, **47**, 8166

27. M. Glinchuk, E. Eliseev, A. Morozovska and R. Blinc, *Phys. Rev. B*, 2008, **77**, 024106.

28. M.Q. Cai, Y. Zheng, B. Wang and G.W. Yang, *Appl. Phys. Lett.*, 2009, **95**, 232901.

29. D. Ghosh, H. Han, J.C. Nino, G. Subhash, and J.L. Jones, *J. Am. Ceram. Soc.*, 2012, **95**, 2504

30. M.T. Buscaglia, V. Buscaglia, M. Viviani, and P. Nanni, *J. Am. Ceram. Soc.*, 2001, **84(2)**, 376

31. G. Sreenivasulu, M. Popov, F. A. Chavez, S. L. Hamilton, P.R. Lehto and G. Srinivasan, *Appl. Phys. Lett.*, 2014, **104**, 052901

32. R.K. Kotnala, V. Gupta, and K.C. Verma, *Curr. Appl. Phys.*, 2014, **14**, 749

33. G. Sreenivasulu, M. Popov, F.A. Chavez, S.L. Hamilton, P.R. Lehto, and G. Srinivasan, *Appl. Phys. Lett.*, 2014, **104**, 052901

34. M. Lorenz, V. Lazenka, P. Schwinkendorf, F. Bern, M. Ziese, H. Modarresi, A. Volodin,

M.J.V. Bael, K. Temst, A. Vantomme and M. Grundmann, *J. Phys. D: Appl. Phys.*, 2014, **47**, 135303

35. K.C. Verma, V. Gupta, J. Kaur and R.K. Kotnala, J. Alloys Compd., 2013, **578**, 5

36. M. Callsen, V. Caciuc, N. Kiselev, N. Atodiresei and S. Blugel, *Phys. Rev. Lett.*, 2013, **111**, 106805.

37. S. Neeleshwar, C.L. Chen, C.B. Tsai, Y.Y. Chen, and C.C. Chen, *Phys. Rev. B*, 2005, **71**, 201307.

38. S.K. Upadhyay and V.R. Reddy, *J. Appl. Phys.*, 2013, **113**, 114107.

39. J.F. Moulder, W.F. Stickle, P.E. Sobol and K.D. Bomben, *Handbook of X-ray Photoelectron Spectroscopy* (Physical Electronics, Reissue edition, 1995).

40. S.Y. Seo, C.H. Kwak, Y.B. Lee and S.H. Kim, *J. Korean Phys. Soc.*, 2008, **52**, 805

41. C.X. Li, B. Yang, S.T. Zhang, D.Q. Liu, R. Zhang, Y. Sun, W.W. Cao, *J. Alloys Comp.*, 2014, **590**, 346

42. X. Lu, Y. Kim, S. Goetze, X. Li, S. Dong, P. Werner, M. Alexe and D. Hesse, *Nano Lett.*, 2011, **11**, 3202

43. J.E. Spanier, A.M. Kolpak, J.J. Urban, I. Grinberg, L. Ouyang, W.S. Yun, A.M. Rappe and H.Park, *Nano Lett.*, 2006, **6**, 735

44. Z.X. Cheng, H. Shen, J.Y. Xu, P. Liu, S.J. Zhang, J.L. Wang, X.L. Wang and S.X. Dou, *J. Appl. Phys.*, 2012, **111**, 034103

45. J. Ma, J. Hu, Z. Li and C.W. Nan, *Adv. Mater.*, 2011, **23**, 1062.

46. V.G. Bary'achtar, V.A. L'vov, and D.A. Jablonskii, *JETP Lett.*, 1983, **37**, 673.

47. E.V. Ramana, F. Fiqueiras, M.P.F. Graca and M.A. Valente, *Dalton Trans.*, 2014, **43**, 9934

48. R.C. Kambale, K.M. Song and N. Hur, Curr. *Appl. Phys.*, 2013, **13**, 562

49. M. Liu, O.J. Lou, S. Li, X. Xing, G. Yang, N. X. Sun, *J. Appl. Phys.*, 2011, **109**, 07D913.

50. E. A. Eliseev, A. N. Morozovska, M. D. Glinchuk, R. Blinc, *Phys. Rev. B*, 2009, **79**, 165433.

51. O.G. Udalov, N.M. Chtchelkatchev and I. S. Beloborodov, Phys. Rev. B, 2014, **89**, 174203

52. L. Chotorlishvili, R. Khomeriki, A. Sukhov, S. Ruffo and J. Berakdar, *Phys. Rev. Lett.*, 2013, **111**, 117202

53. N. Sedlmayr, V.K. Dugaev and J. Berakdar, *Phys. Rev. B*, 2009, **79**, 174422

54. H. Katsura, N. Nagaosa and A.V. Balatsky, *Phys. Rev. Lett.*, 2005, **95**, 057205

55. G. Anjum, S. Mollah, D.K. Shukla, and R. Kumar, *Mater. Lett.*, 2010, **64**, 2003.

56. H. Zheng, J. Wang, S.E. Lofland, Z. Ma, L.M. Ardabili, T. Zhao, L.S. Riba, S.R. Shinde, S.B. Ogale, F. Bai, D. Viehland, Y. Jia, D.G. Schlom, M. Wuttig, A. Roytburd, and R. Ramesh, *Science*, 2004, **303**, 661.

57. N.A. Pertsev, A.G. Zembilgotov, and A.K. Tagantsev, *Phys. Rev. Lett.*, 1998, **80**, 1988.

58. A.G. Zembilgotov, N.A. Pertsev, U. Bottger, and R. Waser, *Appl. Phys. Lett.*, 2005, **86**, 052903.

59. X. Chen, Z. Liu, Q. Sun, M. Ye, and F. Wang, *Optics Commun.*, 2011, **284**, 2046.

60. Q. Sun, X. Chen, Z. Liu, F. Wang, Z. Jiang, and C. Wang, *J. Alloys Compd.*, 2011, **509**, 5336

61. X. Li, Y. Hou, Q. Zhao, and L. Wang, *J. Colloid Interface Sci.*, 2011, **358**, 102

Figure Captions

Fig.1 XRD pattern of xBaTiO$_3$ - (1-x)ZnFe$_2$O$_4$ (BTZF) [x = 0.25 (BTZF2575), 0.35(BTZF3565), 0.45(BTZF4555), 0.50(BTZF5050) and 0.75(BTZF7525)] nanostructure composites measured at room temperature.

Fig.2 (a) TEM image (left) and HRTEM image (right) of BTZF2575, BTZF3565 and BTZF4555 sample, respectively. Inset of HRTEM image is the SAED pattern of each respective sample.

Fig. 2 (b) TEM image (left) and HRTEM image (right) of BTZF5050 and BTZF7525 sample, respectively. Inset of HRTEM image is the SAED pattern of each respective sample.

Fig.3 (a-e) Magnetization (M) versus magnetizing field (H_{dc}) of BTZF nanostructures (Inset shows the polarization (P) versus electric field (E) of the respective sample. (f) Plot of M and remanent polarization, P_r with varying the concentration of BT in BTZF composite.

Fig.4 XPS spectra of Fe 2p of BTZF nanostructure measured at room temperature.

Fig.5 ME voltage coefficient (α_E) with H_{dc} (0 - 6 kOe) under the influence of H_{ac} = 5 Oe and frequency of 1093 Hz of BTZF nanostructure.

Fig. 6 MD responses of the BTZF nanostructure under the influence of H_{dc} (0 - 6 kOe) at 1 kHz of frequency.

Fig. 7 Fluorescence spectra of BTZF nanostructure measured at room temperature.

Table1. Values of lattice parameters *a* and *c* of BT and *a* of ZF, and diameter (*d*), length (*l*), saturation magnetization (M_s), remanent magnetization (M_r), magnetic coercive field (H_c), spontaneous polarization (P_s), remanent polarization (P_r), electric coercive field (E_c), magnetoelectric coefficient (α_E) at 3 kOe and Magnetocapacitance (MC) at 3 kOe of BTZF nanostructures.

BTZF	Lattice constant			Multiferroic properties									
	BT		ZF	BTZF									
	a(Å)	*c*(Å)	*a*(Å)	*d* (nm)	*l* (nm)	M_s (emu/g)	M_r (emu/g)	H_c (Oe)	P_s (μC/cm^2)	P_r (μC/cm^2)	E_c (kV/cm)	α_E (mV/cmOe)	MC (%)
2575	4.0013	4.1992	8.448	6	>100	0.19	0.056	1068	69.61	18.44	13.79	122.9	2.84
3565	3.992	4.0274	8.438	33	103	15.41	3.19	319	41.95	5.47	1.78	30.5	1.24
4555	3.992	4.0222	8.432	54	120	8.71	1.38	255	26.31	5.36	3.61	29.2	0.78
5050	3.995	4.0304	8.422	59	141	0.15	0.038	249	31.66	6.41	12.81	51.7	1.42
7525	3.999	4.0378	8.351	84	-	0.25	0.047	116	26.10	12.51	12.93	43.9	1.12

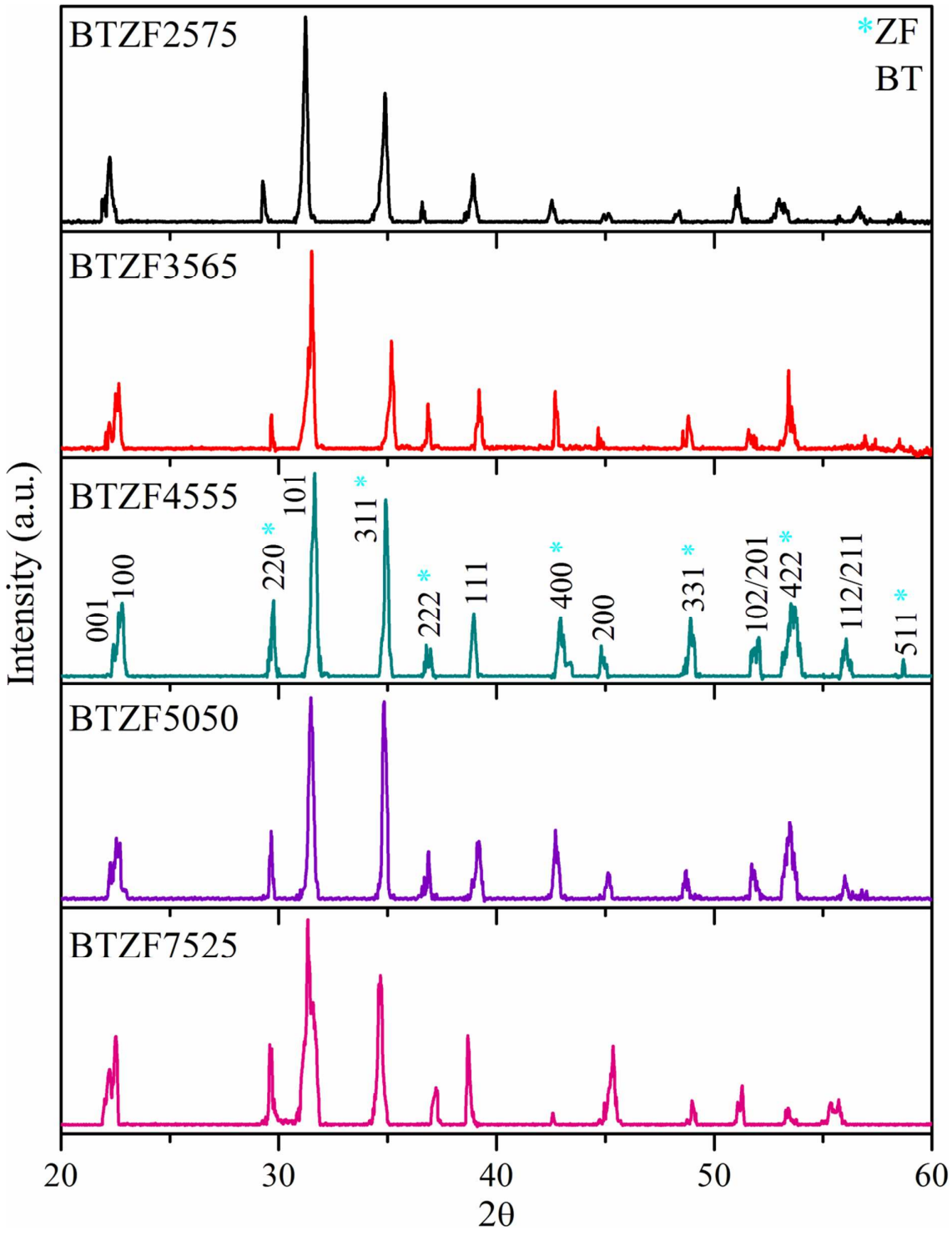

Fig.1

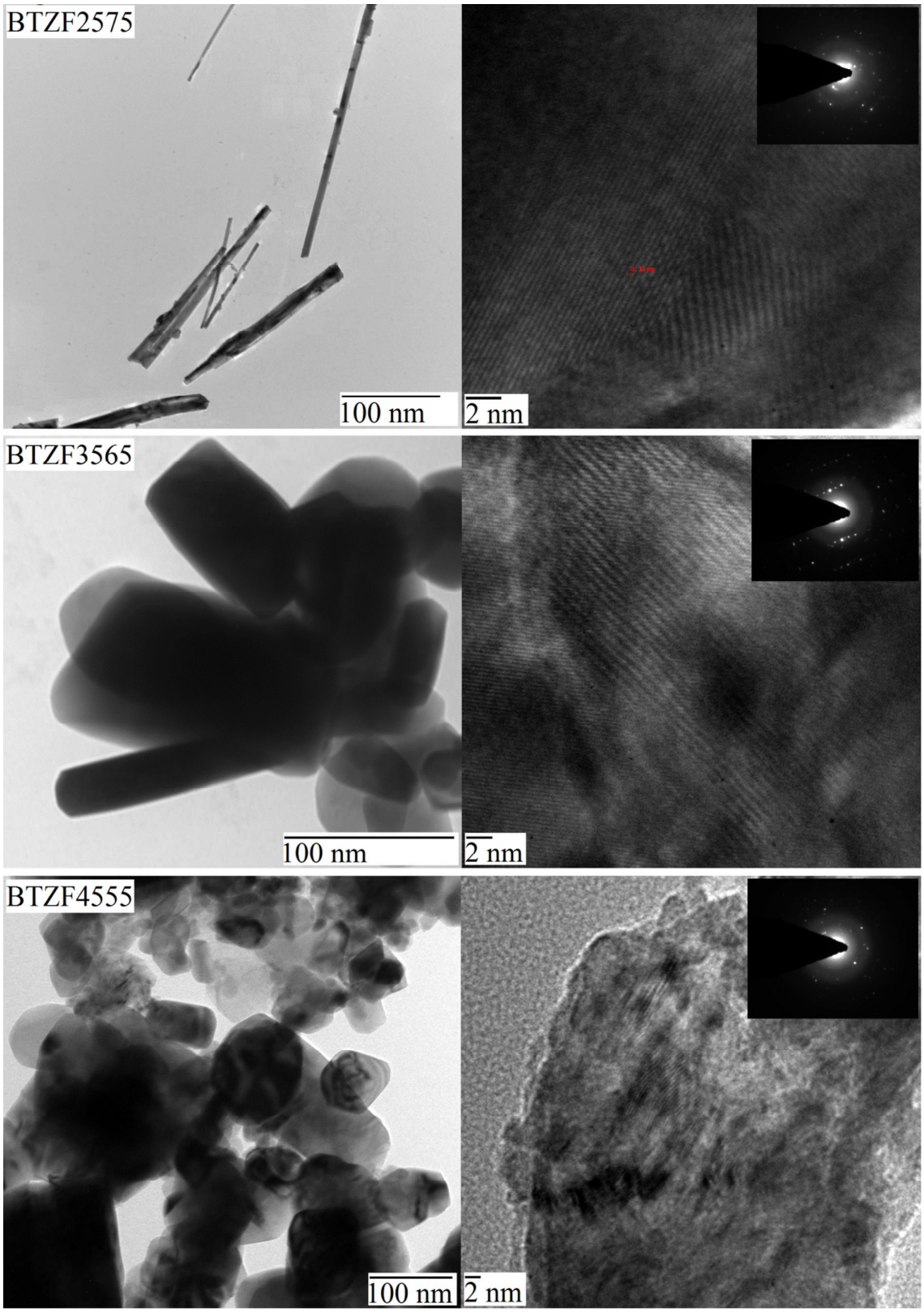

Fig.2(a)

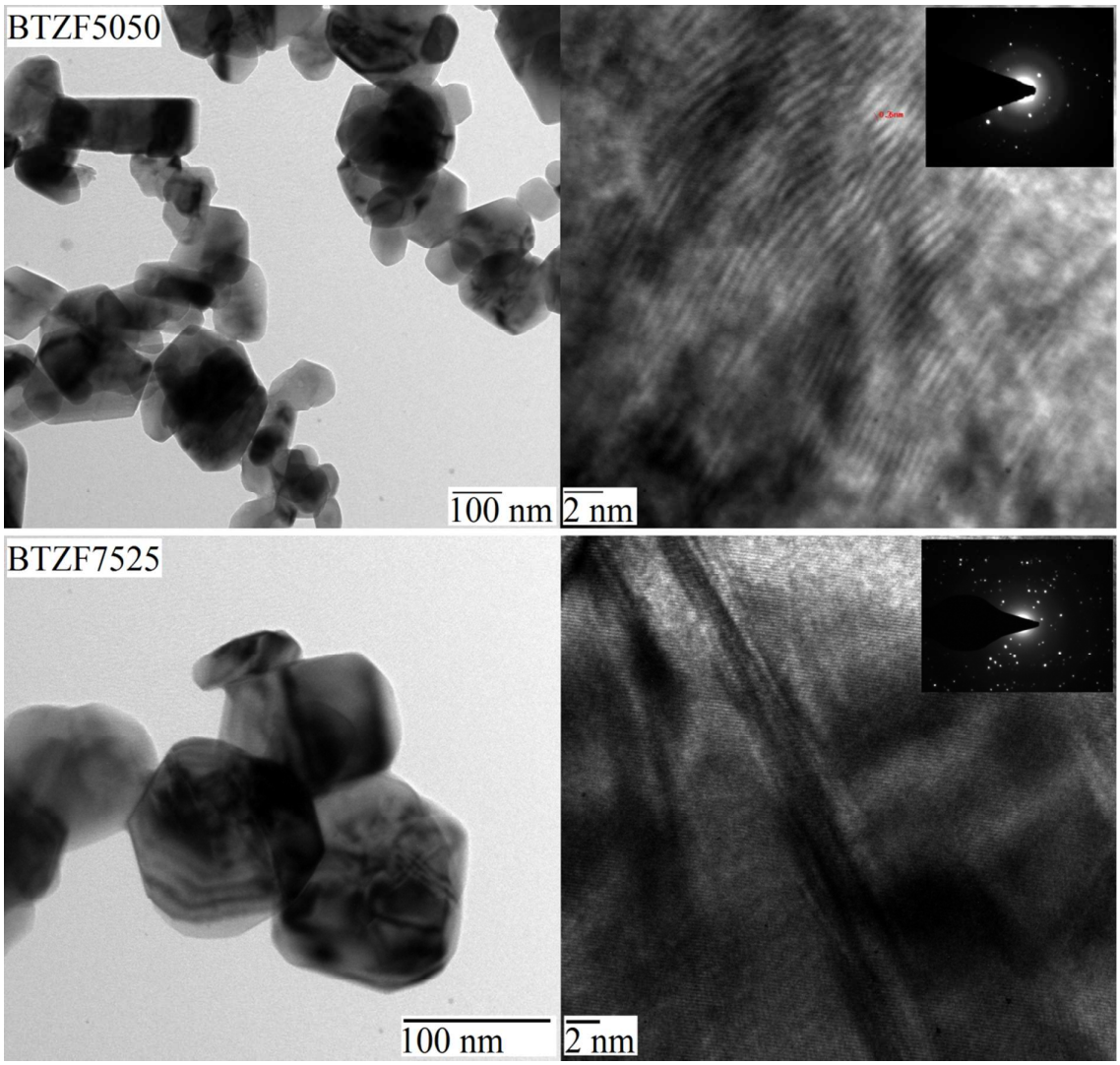

Fig.2(b)

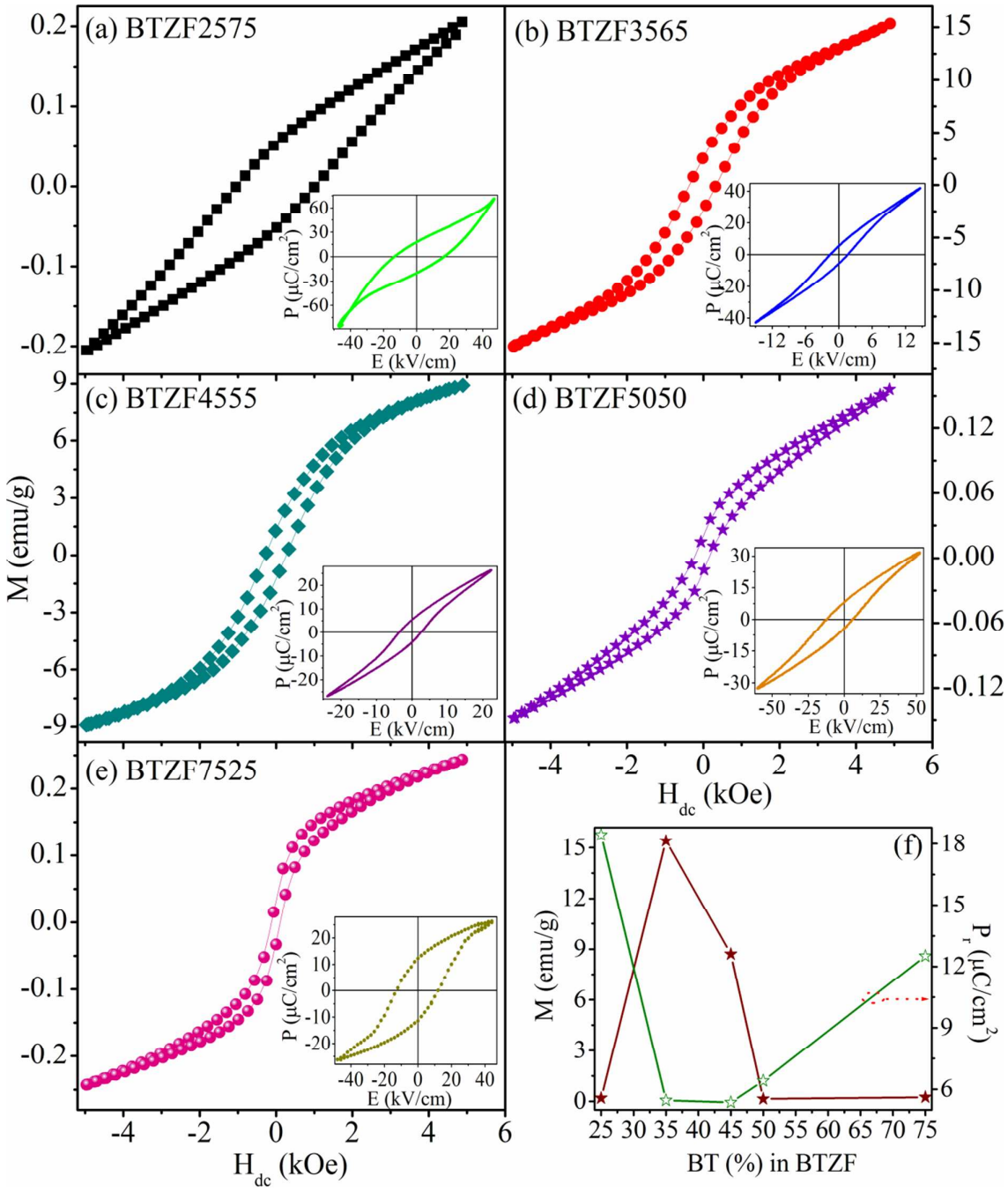

Fig.3

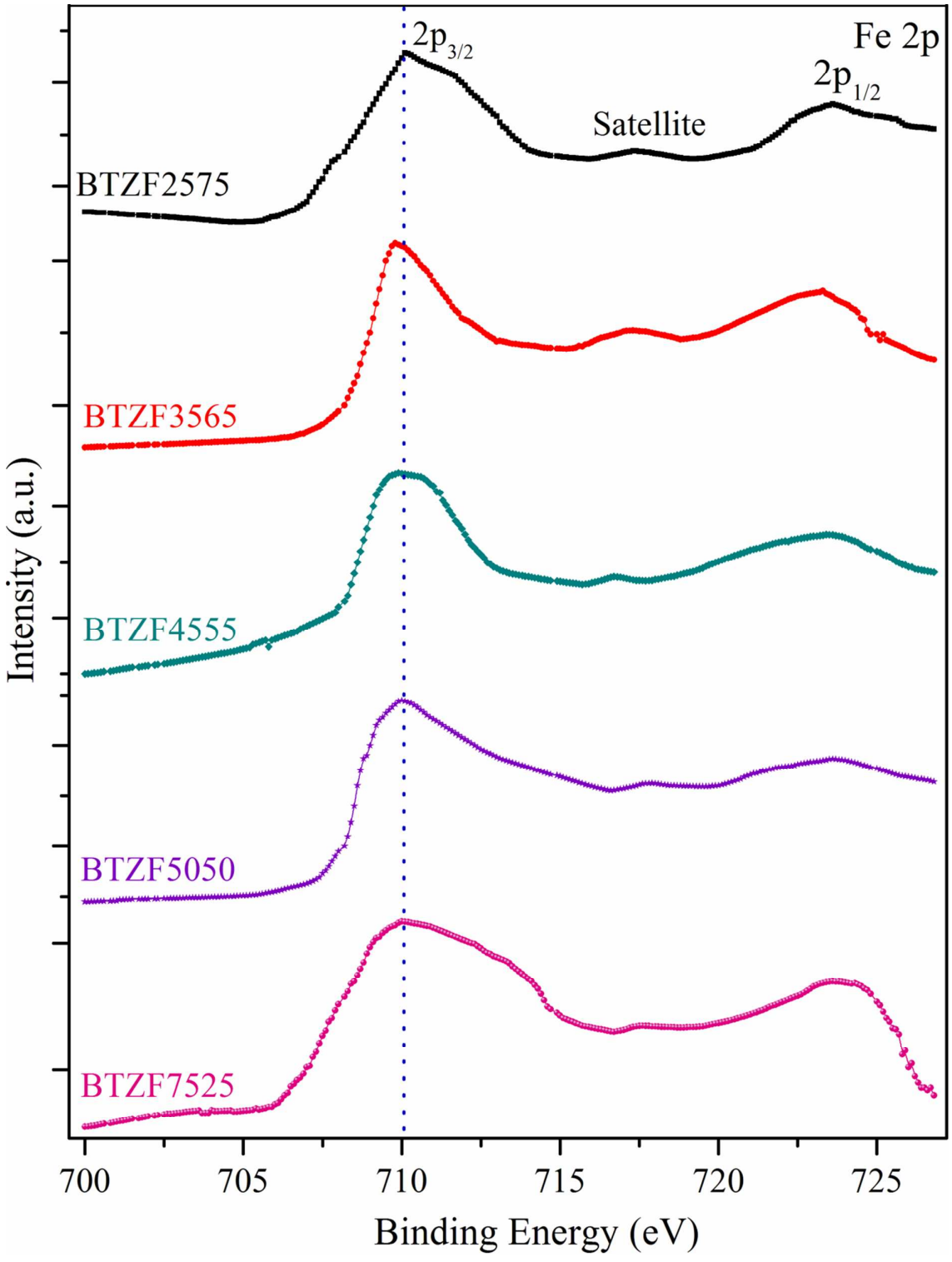

Fig.4

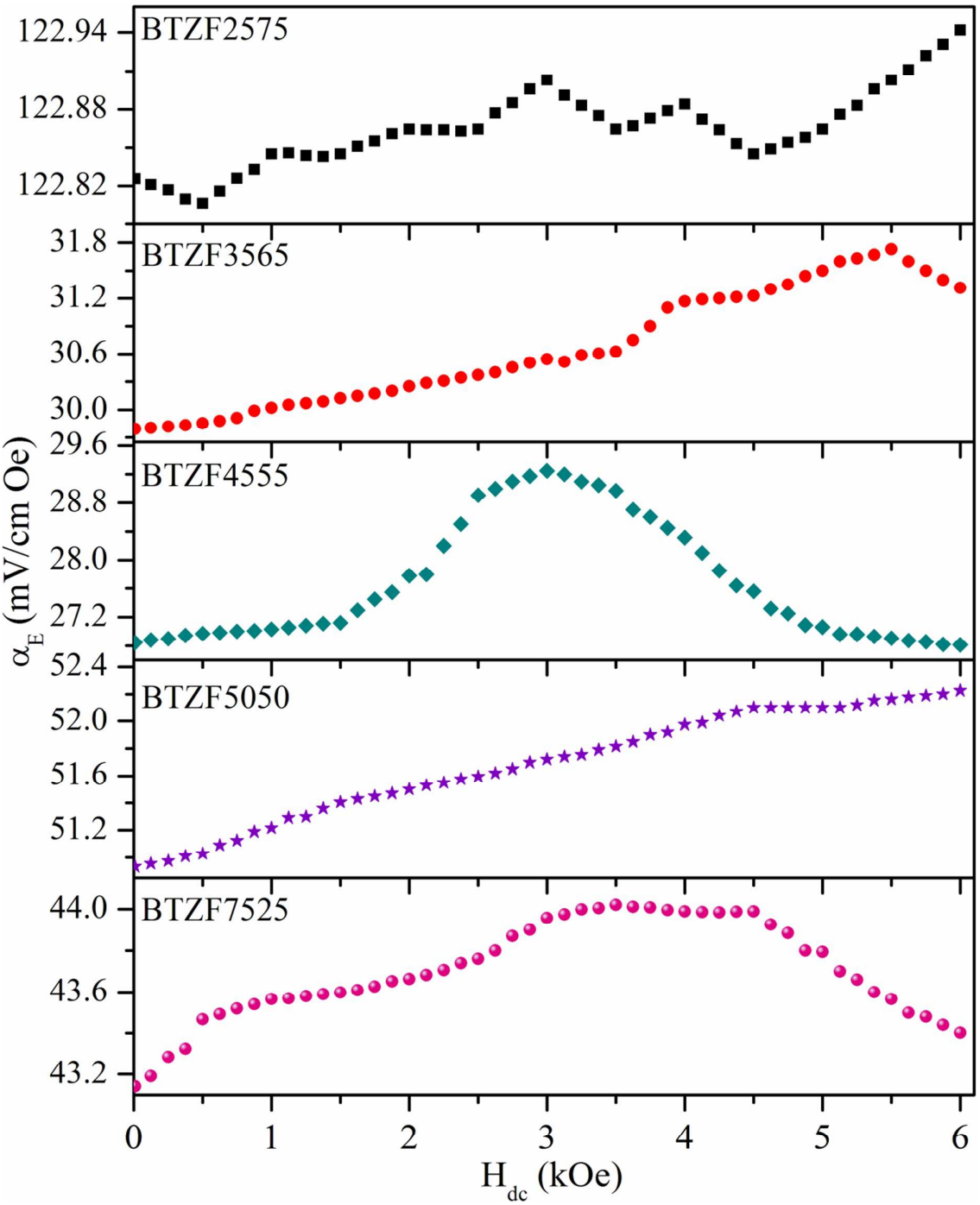

Fig.5

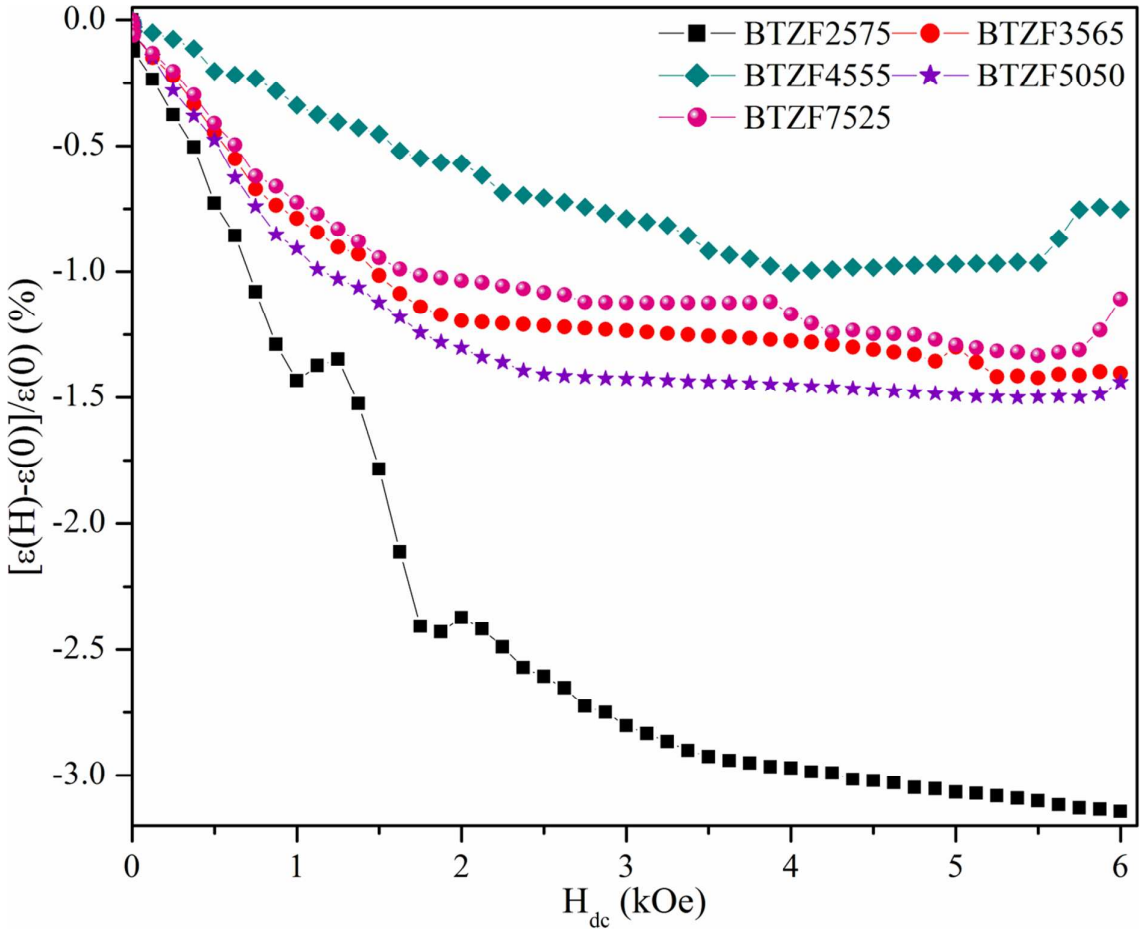

Fig.6

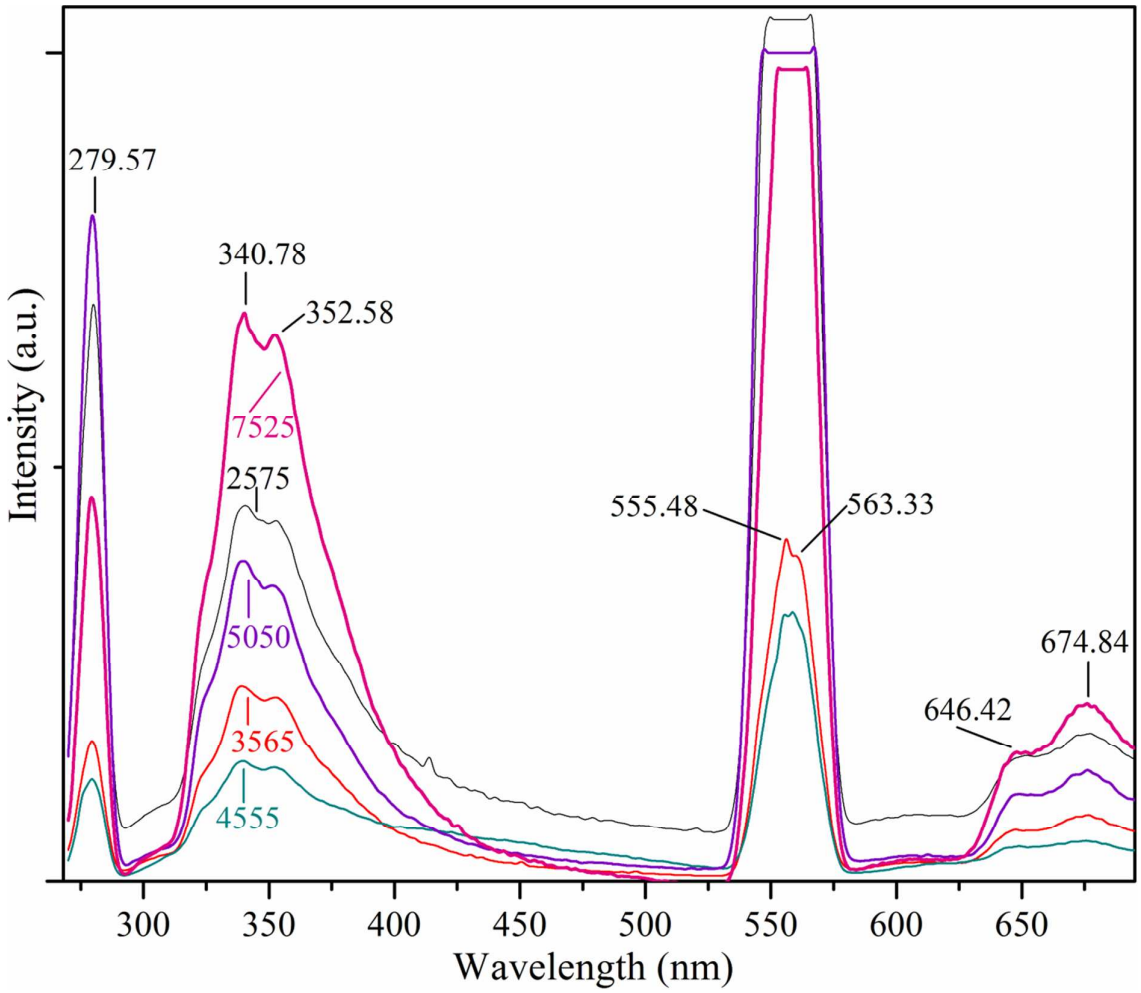

Fig.7